JACS
JOURNAL OF THE AMERICAN CHEMICAL SOCIETY
pubs.acs.org/JACS
Article

Colloidal Germanium Quantum Dots with Broadly Tunable Size and Light Emission

Jungchul Noh, Hyun Gyung Kim, Daniel W. Houck, Tushti Shah, Yangning Zhang, Alexandra Brumberg, Richard D. Schaller, and Brian A. Korgel*

Cite This: J. Am. Chem. Soc. 2025, 147, 1792−1802
Read Online
ACCESS | Metrics & More | Article Recommendations | Supporting Information

ABSTRACT: Germanium (Ge) colloidal quantum dots (CQDs) were synthesized by thermal decomposition of GeI_2 using capping ligand mixtures of oleylamine (OAm), octadecene (ODE), and trioctylphosphine (TOP). Average diameters could be tuned across a wide range, from 3 to 18 nm, by adjusting reactant concentrations, heating rates, and reaction temperatures. OAm promotes decomposition of GeI_2 to Ge and serves as a weakly bound capping ligand. ODE displaces OAm during the reaction to terminate particle growth and prevent surface oxidation. TOP is necessary for obtaining nanocrystals larger than 11 nm. The Ge CQDs have relatively narrow size distributions and exhibit size-dependent, band-edge photoluminescence (PL), with peak energies from 0.8 to 1.34 eV, across a wide spectral range in the infrared (IR).

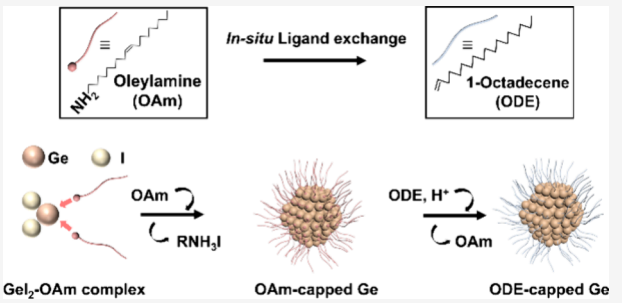

1. INTRODUCTION

Size-dependent infrared (IR) optical properties of germanium (Ge) colloidal quantum dots (CQDs) have been a topic of interest for more than two decades.[1−15] Many synthetic approaches have been explored, including solution-phase methods involving Ge halides ($GeCl_4$, $GeBr_2$, GeI_2, or GeI_4),[16−21] $Ge[N(Si(Me_3)_2]_2$[22] mixtures of GeI_2 and GeI_4,[23,24] polymerization of $[Ge_9]^{4-}$ or other related Zintl ions,[24] akylgermanes,[25] and sulfur-assisted thermal decomposition of triphenyl germanium chloride.[26] Ge nanocrystals have been made by electroless deposition on Ag nanocrystals,[27] thermal decomposition of Ge oxides,[28,29] and aerosol processes.[30−33] Ge nanorods and nanowires have also been made by metal seed-mediated vapor−liquid−solid (VLS), solution−liquid−solid (SLS) and supercritical fluid−liquid−solid (SFLS) growth.[34−38] In most cases, these Ge CQDs have fallen short of achieving luminescence in the IR range at room temperature. In some cases, Ge CQDs have exhibited band edge, red and near-IR photoluminescence (PL), but with very limited size-dependent color tunability.[3,8,23,34,39−46] Here, we report a synthetic approach to Ge CQDs that yields widely tunable sizes, average diameters ranging from 3 to 18 nm, uniform size distributions and band edge, room temperature PL spanning a wide range of IR wavelengths.

The approach relies on a heat-up method in which Ge CQD nucleation and growth is initiated by decomposition of GeI_2 in oleylamine (OAm). OAm serves as a weak reducing agent for GeI_2 and as a capping ligand for the nanocrystals. Nucleation begins to occur at relatively low temperatures around 120 °C. The labile Ge-amine bonding allows the nanocrystals to grow as the mixture is heated. Octadecene is also added to the reaction mixture to serve as a capping ligand. At lower growth temperatures, the alkenes do not react with the Ge surface, but once the reaction temperature reaches about 260 °C, CQD growth is terminated by ODE addition to the nanocrystal surface. ODE displaces OAm to yield a layer of covalent irreversible Ge−C bonded ligands as shown in Figure 1. To obtain nanocrystals with diameters larger than 11 nm, trioctylphosphine (TOP) is also added to enhance the nanocrystal growth kinetics. This approach of a heat-up method with in situ ligand exchange with ODE allows the size of the nanocrystals to be widely tuned using reaction temperature, time and reactant concentrations. The ODE-capped Ge CQDs are resistant to oxidation and exhibit size-dependent, band-edge PL over a wide spectral range. This synthetic strategy helps to position Ge CQDs as a promising alternative to lead- and mercury-based semiconductor nanocrystals for IR optical and optoelectronic applications.

2. EXPERIMENTAL DETAILS

2.1. Chemicals. Germanium diiodide (GeI_2, >95%) was purchased from Gelest and used as received in a nitrogen-filled glovebox. Trioctylphosphine (TOP, 98%), 1-octadecene (ODE,

Received: September 30, 2024
Revised: December 10, 2024
Accepted: December 10, 2024
Published: January 3, 2025

https://doi.org/10.1021/jacs.4c13692
J. Am. Chem. Soc. 2025, 147, 1792−1802

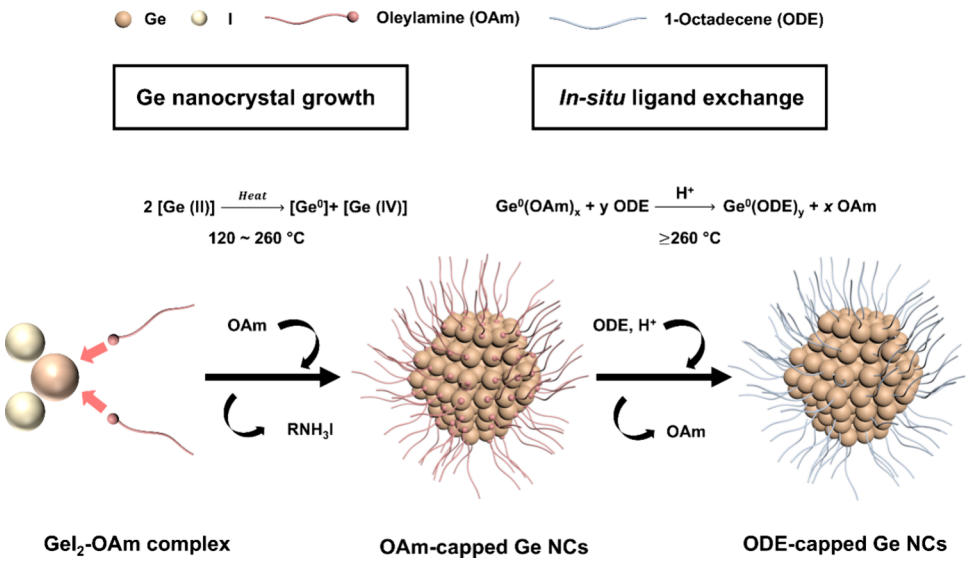

Figure 1. Synthetic pathway for ODE-capped Ge CQDs. As a solvent mixture with GeI_2 and OAm is heated, OAm induces GeI_2 decomposition to Ge at about 120 °C to initiate nanocrystal nucleation and growth. OAm serves as a reversibly bonded ligand that allows particle growth as the reaction mixture is heated. Once the temperature reaches 260 °C, hydrogermylation ensues between ODE and the Ge surface, displacing OAm and terminating nanocrystal growth.

Table 1. Experimental Conditions Used to Generate Ge Nanocrystals, Including the Amounts of GeI_2, OAm, ODE, and TOP, the Final Reaction Temperature and the Heat-Up Rate[a]

#	GeI_2 (g)	OAm (mL)	ODE (mL)	TOP (mL)	temp. (°C)	heat-up (°C/min)	diameter from TEM (nm)	diameter from SAXS (nm)[b]
1	0.20	30	10		300	5	3.0 ± 0.3	3.0 ± 0.2
2	0.30	30	10		300	5	6.3 ± 0.7	6.2 ± 0.8
3	0.30	25	10		300	5	8.8 ± 0.7	8.8 ± 0.8
4	0.30	20	10		300	5	10.2 ± 1.1	10.2 ± 1.1
5	0.30	20	8	4	300	5	12.0 ± 1.0	11.8 ± 1.2
6	0.30	20	8	8	300	5	15.2 ± 1.7	15.4 ± 1.9
7	0.30	20	8	12	300	5	18.0 ± 1.9	17.8 ± 1.8
8	0.30	20			300	5	5.6 ± 2.2	
9	0.40	20		10	300	5	50−100	
10	0.30	20	10		180	5	2.3 ± 0.2	
11	0.30	20	10		200	5	4.8 ± 0.5	
12	0.30	20	10		220	5	5.3 ± 0.7	
13	0.30	20	10		240	5	6.6 ± 1.0	
14	0.30	20	10		260	5	9.7 ± 1.3	
15	0.30	20	10		280	5	9.9 ± 1.3	
16	0.30	20	10		300	17	2.6 ± 0.7	
17	0.30	20	10		300	12	5.3 ± 1.2	
18	0.30	20	10		300	8	7.9 ± 1.6	
19	0.30	20	10		300	3	11.4 ± 1.3	

[a]Reaction mixtures were held at the final temperature for 1 h. Average diameters of the nanocrystals were determined by TEM and SAXS [b]SAXS measurements were only performed for samples with the reported diameters.

98%), tetrachloroethylene (TCE, anhydrous), chloroform-*d* ($CDCl_3$, 99.8 atom % d), and toluene (anhydrous) were purchased from Sigma-Aldrich. Oleylamine (OAm, >98%) was obtained from AkzoNobel Company. Absolute ethanol (EtOH) was purchased from Fischer Scientific. All chemicals were used without further purification.

2.2. Ge Nanocrystal Synthesis. OAm, TOP and ODE were added to a three-neck flask on a Schlenk line and degassed under vacuum for 1 h at 110 °C. The reactant amounts used in this study are summarized in Table 1. The flask was transferred into a nitrogen-filled glovebox for the addition of GeI_2, then removed from the glovebox and placed back on the Schlenk line to be degassed under vacuum for 1 h at 110 °C. The reaction mixture was heated to a desired final reaction temperature, then removed from the heating mantle and allowed to cool to room temperature. Ge nanocrystals were isolated by precipitation with 20 mL of EtOH and centrifugation at 8000 rpm (8228 rcf) for 5 min. The supernatant was discarded and the nanocrystal product was redispersed in 15 mL of toluene. After adding 15 mL of EtOH, the mixture was centrifuged again at 8000 rpm for 5 min. This precipitative washing procedure was repeated two more times. The nanocrystal product was finally dispersed in toluene and centrifuged at 8000 rpm for 5 min to remove any poorly capped nanocrystals. Nanocrystals were redispersed in toluene and stored in a glovebox. Typical reactions yielded 100−150 mg of nanocrystal product, including the ligand contribution. The molar conversion of GeI_2 to Ge in the reactions based on the weight percentage of ligand in the sample determined by thermal gravimetric analysis (TGA) is 40−50% (see Supporting Information, Figure S8).

https://doi.org/10.1021/jacs.4c13692
J. Am. Chem. Soc. 2025, 147, 1792−1802

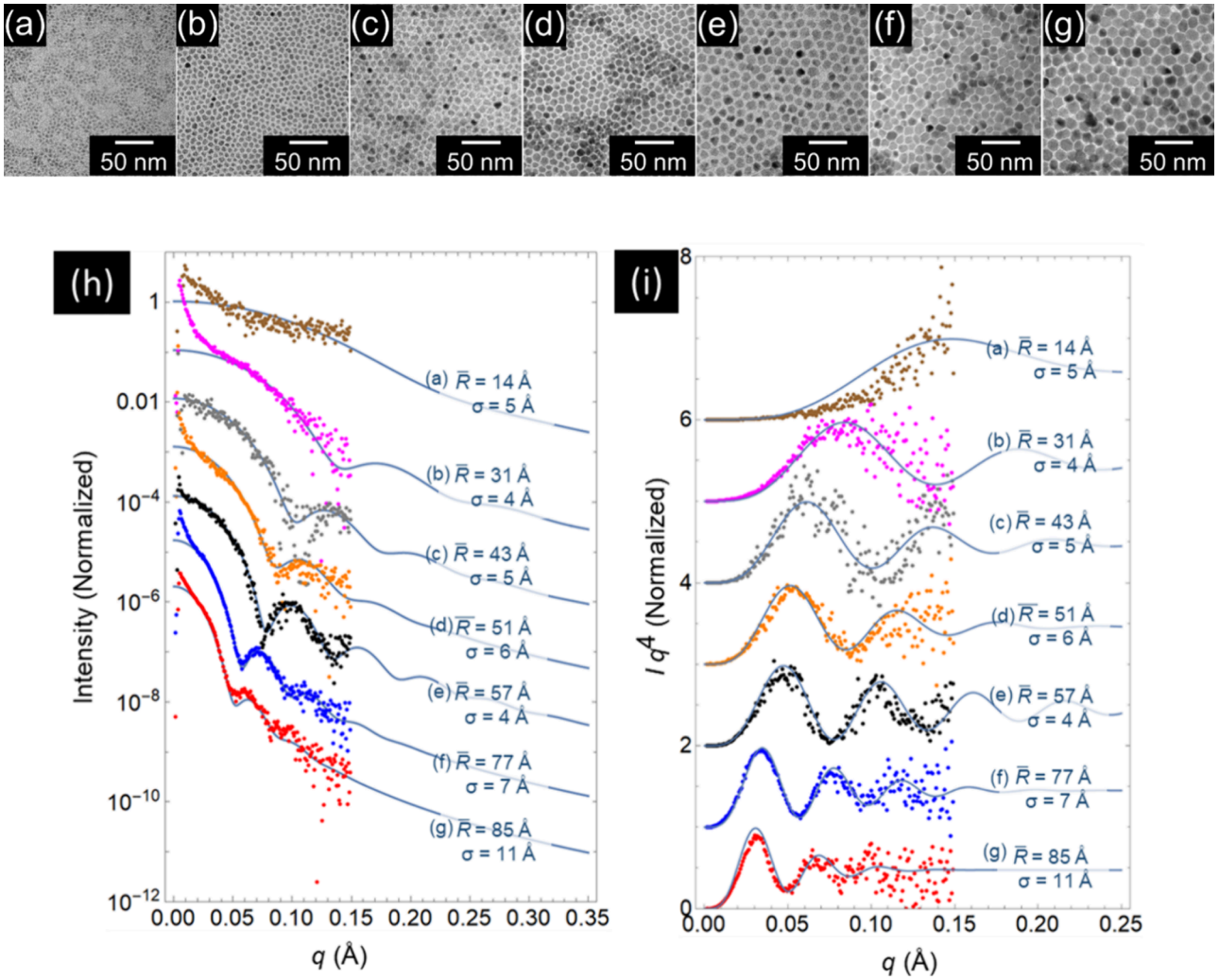

Figure 2. TEM images of Ge nanocrystals produced using the reaction conditions shown in Table 1. Reaction conditions and average diameter of the nanocrystals in each image were (a) #1, 3.0 ± 0.3, (b) #2, 6.3 ± 0.7, (c) #3, 8.8 ± 0.7, and (d) #4, 10.2 ± 1.1 nm. With the fixed molar ratio of GeI_2:OAm (1:66.1), adding 4, 8, 12 mL of TOP resulted in Ge nanocrystals with the particle size of (e) 12.0 ± 1.0, (f) 15.2 ± 1.7, and (g) 18.0 ± 1.9 nm. Histograms are provided in Supporting Information (Figure S6). (h,i) SAXS data for the nanocrystals imaged in (a−g). The curve fits shown in blue correspond to best fits of Eqs 1−3 to the scattering data. The Porod plots in (i) were fit to Eqs 1−3 to obtain the average diameters and standard deviation of each sample: (i) 17.8 ± 1.8, (ii) 15.4 ± 1.9, (iii) 11.8 ± 1.2, (iv) 10.2 ± 1.1, (v) 8.8 ± 0.8, (vi) 6.2 ± 0.8, and (vii) 3.0 ± 0.2 nm.

2.3. Materials Characterization. Transmission electron microscopy (TEM) images were obtained with a FEI Tecnai Spirit Bio Twin or a FEI Titan G2 ChemiSTEM operated at 80 kV. The nanocrystals were drop-cast from toluene onto continuous carbon-coated Cu grids (Electron Microscopy Science) and placed under vacuum at 60 °C overnight to reduce carbon contamination. Annular dark-field scanning electron microscopy (ADF-STEM) was performed using a JEOL NEOARM equipped with a probe corrector operated at an accelerating voltage of 80 kV. Nanocrystals were drop-cast from toluene onto continuous carbon-coated Cu grids and dried under vacuum at 80 °C overnight. After placing the sample on the TEM holder, UV cleaning was performed for 10 min using a Hitachi UV/Ozone cleaner prior to imaging.

Scanning electron microscopy (SEM) images were acquired using a Zeiss SUPRA 40VP SEM at 3 keV with an in-lens detector. Nanocrystals were deposited on a polished Si wafer (Virgina Semiconductor, undoped, >100 Ω cm) coated with ∼1 nm of Ir. The Ir was deposited on the wafer using a Cressington 208 HR sputter coater operated at 20 mA.

Contact angle measurements were obtained by placing a water droplet onto a Ge nanocrystal film on a double side polished Si wafer (Vergina Semiconductor, undoped, >100 Ω cm). Prior to depositing the nanocrystal layer, the Si wafer (1×1 cm^2) was sonicated in EtOH for 10 min. The Ge nanocrystals dispersed in toluene (5 mg/mL) were drop-cast onto Si wafers and allowed to dry in a glovebox overnight. Images of the sessile water droplets were obtained using a Ramé-hart, 500-U4 contact angle goniometer.

Raman spectra were measured using a Witec Micro-Raman Spectrometer Alpha 300 with 532 nm laser excitation (7 mW). Nanocrystals were evaporated on 2.5 × 2.5 cm^2 Al foil substrates and spectra were acquired for 5 s.

X-ray diffraction (XRD) was performed using a Rigaku R-Axis Spider X-ray diffractometer with Cu Kα radiation (λ = 1.541 Å) in the 2θ range of 20−80°. Data were collected from dried nanocrystals on a 0.5 mm nylon loop for 7 min with an image plate detector. The two-dimensional powder patterns were converted to one-dimensional patterns with the Rigaku 2DP powder processing program.

Small angle X-ray scattering (SAXS) was carried out on a Xenoc SAXSLAB with a Cu Kα radiation (λ = 1.541 Å) and Pilatus3 R 300k image plate detector (487 × 619 pixels with an area of 0.172 × 0.172 mm^2 per pixel). Ge nanocrystals were dispersed in toluene at a concentration of 5 mg/mL in epoxy-sealed capillary tubes loaded into a vacuum chamber. A sample-to-detector distance was 1084 mm, and SAXS data were acquired for 1500 s. 2D SAXS images were converted

https://doi.org/10.1021/jacs.4c13692
J. Am. Chem. Soc. 2025, 147, 1792−1802

to 1D spectra using SAXSGUI software (version 2.15). The solution SAXS data were solvent background corrected. The data are fit to the calculated scattering intensity expected for a collection of non-interacting solid spheres[47,48]

$$I(q) \propto \int_0^\infty N(R)P(qR)R^6 dR \quad (1)$$

where $N(R)$ is the nanocrystal size distribution, which is taken to be Gaussian with average radius $\overline{R}$ and standard deviation σ

$$N(R) = \frac{1}{\sigma\sqrt{2\pi}}\exp\left[\frac{-(R-\overline{R})^2}{2\sigma^2}\right] \quad (2)$$

and the form factor $P(qR)$, which for a homogeneous sphere is

$$P(qR) = 3\left[\frac{\sin(qR) - qR\cos(qR)}{(qR)^3}\right]^2 \quad (3)$$

^{1}H NMR spectra were recorded using a Varian MR 400 spectrometer at 400 MHz, using a 90° pulse width, a 2 s relaxation delay, and 128 scans. Ge nanocrystals were dispersed in chloroform-*d* at a concentration of 5 mg/mL in a 5 mm NMR tube. Data were processed using MestReNova software for background correction.

Attenuated total reflectance Fourier transform infrared (ATR-FTIR) spectroscopy was performed using a Thermo Mattson Infinity Gold FTIR spectrometer with a Spectra-Tech Thermal ARK attenuated total reflectance module. Nanocrystals dispersed in toluene at a concentration of 5 mg/mL were drop-cast onto the crystal plate of the ARK module. The sample and detector chambers were purged with N_2 for 30 min to eliminate CO_2 background signal. Spectra were acquired with 512 scans at a resolution of 4 cm^{-1}.

X-ray photoelectron spectroscopy (XPS) was performed on a Kratos Axis Ultra X-ray photoelectron spectrometer with monochromatic Al Kα radiation ($h\nu$ = 1486.5 eV) at 150 W (10 mA and 15 kV). Nanocrystals were drop-cast from toluene onto a conductive boron-doped silicon wafer (GlobiTech, 0.01−0.02 Ω cm). Casa XPS software was used for peak deconvolution, by fitting the peaks to a Gaussian distribution and a Shirley background function. Sample charging was corrected by shifting the C 1s peaks to a value expected of hydrocarbons at 284.8 eV.

UV-vis-NIR absorbance spectra were recorded with a Cary 5000 UV-vis-NIR spectrophotometer using quartz cuvettes with 1.0 cm path length. The Ge nanocrystals were dispersed in anhydrous TCE to avoid near-infrared light absorption by C−H vibrations of solvents. All reported spectra have been solvent background-subtracted.

Photoluminescence (PL) spectra were acquired on a home-built InGaAs detector, using a PicoQuant laser diode with 450 nm as the excitation wavelength. Nanocrystals dispersed in anhydrous TCE were used, and PL quantum yield (QY) was determined relative to the organic dye IR-26 (PL QY = 0.05%) as a standard. For temperature-dependent PL measurements, diluted Ge nanocrystals with average diameter of 8.8 nm were incorporated into poly(methyl methacrylate). The sample was loaded on a sapphire substrate and cooled with liquid helium.

3. RESULTS AND DISCUSSION

3.1. Nanoparticle Crystallinity and Size Control.

Figure 2 shows TEM images and SAXS data for Ge nanocrystals synthesized with average diameters ranging from 3 to 18 nm. The nanocrystals smaller (larger) than 11 nm were produced without (with) TOP. The nanocrystals are relatively uniform with standard deviations about the mean diameter of less than ±15% without size selection. The positive deviation at low q of the scattering data from the scattering profiles calculated using Eqs 1−3 indicates that the nanocrystals are "sticky," although not enough for aggregation to occur.[47−50] The sizes determined from TEM and SAXS are in good agreement.

The use of the heat-up method and the addition of ODE both play an essential role in allowing the size to be manipulated over a wide range while retaining uniform size distributions. Ge nanocrystals can be made by heating up GeI_2 in OAm without ODE; however, these reactions produce nanocrystals with broad size distributions and limited size tunability. Reaction #8 in Table 1 shows the results of a reaction without ODE and Figure 3a shows TEM images of

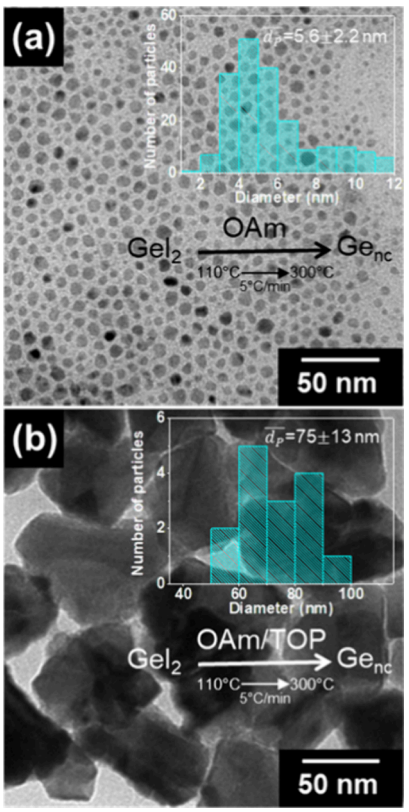

Figure 3. TEM images of Ge nanocrystals obtained from reactions at 300 °C with (a) 0.3 g (0.9 mmol) GeI_2 in 20 mL OAm and (b) 0.4 g (1.2 mmol) GeI_2 in 20 mL OAm and 10 mL TOP. Insets: histograms of the particle size distributions determined from the TEM images.

these nanocrystals. The nanocrystals are relatively polydisperse with an average diameter of 5.6 ± 2.2 nm. Ge nanocrystals can be made by hot injection of GeI_2 (dissolved in OAm) into OAm and ODE at 300 °C, but the resulting nanocrystals are small, with diameters of approximately 2 nm, with very low yields (<10%). ODE forms covalent bonds with Ge and the Ge nanocrystal surface, terminating nanocrystal growth with no ability to obtain larger nanocrystals, which also generates a significant amount of molecular Ge byproduct. Replacing ODE with dodecane—a molecule without an alkene functional group—results in polydisperse Ge nanocrystals with an average diameter of 7.8 ± 2.3 nm (see Supporting Information, Figure S2).

Heating up GeI_2 in OAm and ODE can produce uniform nanocrystals ranging from 3 nm in diameter up to 11 nm, with high reaction yields. The larger nanocrystals are produced using higher temperature and slower heating rates, and/or higher GeI_2 concentrations (see Supporting Information, Figures S3 and S4). For the synthesis of Ge nanocrystals larger than 11 nm, it is necessary to add TOP to the reaction. The presence of TOP in the reaction mixture visibly changes

https://doi.org/10.1021/jacs.4c13692
J. Am. Chem. Soc. 2025, 147, 1792−1802

the GeI_2 decomposition kinetics. For example, the GeI_2 reaction solution is initially orange and turns black as it is heated and nanocrystals begin to form (see Supporting Information, Figure S1). In the absence of TOP, GeI_2 solutions in OAm (or OAm and ODE) turn black when the temperature reaches 120−160 °C. In the presence of TOP, the solution remains orange and does not turn black until the temperature reaches 180−200 °C. TOP appears to interfere with the Ge-OAm bonding and require higher temperatures for reactant decomposition to occur. When nanocrystals do form at the higher temperatures, the growth is enhanced and larger nanocrystals are obtained (see Supporting Information, Figure S5). Decomposition of GeI_2 in OAm and TOP without ODE produces extremely large nanocrystals with diameters of 50−100 nm and irregular shape, as shown in Figure 3b. ODE is again necessary to control the nanocrystal size and uniformity.

All of the reaction conditions shown in Table 1 produced crystalline Ge particles. Figures 4−7 show XRD, HRTEM,

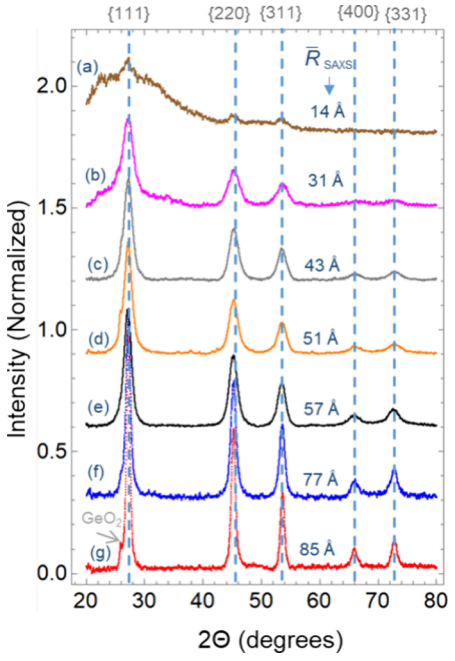

Figure 4. XRD of Ge nanocrystals with different diameters: (a) 3.0 ± 0.2, (b) 6.2 ± 0.8, (c) 8.8 ± 0.8, (d) 10.2 ± 1.1, (e) 11.8 ± 1.2, (f) 15.4 ± 1.9, and (g) 17.8 ± 1.8. CuKα radiation (λ = 1.541 Å) was used. Indexing corresponds to PDF # 00-004-0545 for diamond cubic Ge. Peak broadening from smaller nanocrystals is consistent with Scherrer broadening. In some samples, there is a weak diffraction feature, labeled "GeO_2". This corresponds to the (101) peak of GeO_2. A small amount of oxide impurity was observed in a few of the samples.

ADF-STEM and Raman spectra of Ge CQDs produced under various conditions. The XRD peaks in Figure 4 match diamond cubic Ge (PDF # 00-004-0545) with size-dependent broadening. Minimal GeO_x impurities are observed in the samples, indicating that the alkyl passivation is effective at preventing oxidation. The TEM images in Figure 5 show internal crystallinity of the particles. A fast Fourier transform (FFT) of the TEM image in Figure 5i matches diamond cubic Ge. The average (111), (220), and (311) *d*-spacings from HRTEM and FFT analyses are 0.32, 0.20, and 0.17 nm, respectively, corresponding to a lattice constant of 0.55 nm. The literature value for bulk diamond cubic Ge is 0.566 nm.

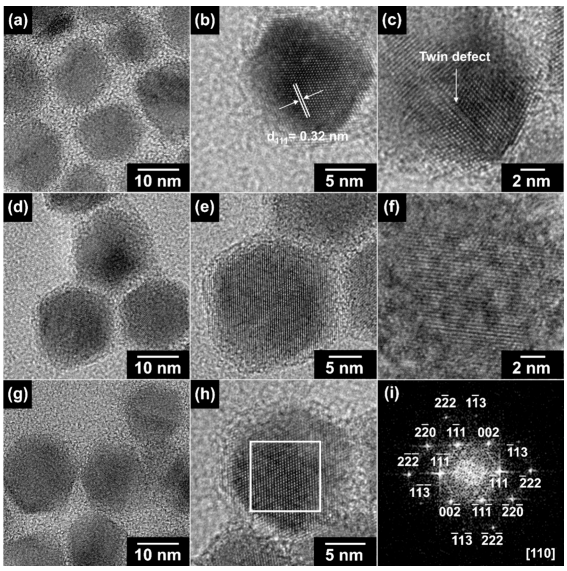

Figure 5. HRTEM images of ODE-capped Ge nanocrystals obtained from Reaction #7 in Table 1. Panels (a), (d), and (g) show HRTEM images of Ge nanocrystals taken at different locations on the TEM grid to illustrate that the size range of this sample is 17.8 ± 1.8. The *d*-spacing shown in (b) of 0.32 nm corresponds to the (111) lattice plane of diamond cubic Ge. High-magnification images of Ge nanocrystals are further shown in (e) and (f). Twin defects are highlighted in (c). (i) FFT of the highlighted region in (h) with indexing corresponding to diamond cubic Ge with [110] zone axis and lattice constant of 0.55 nm.

ADF-STEM images in Figure 6 of some of the larger nanocrystals also show that they are single crystals with

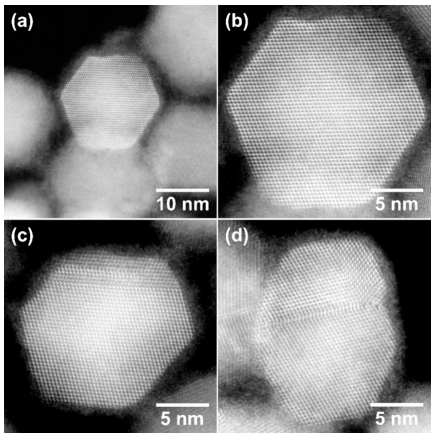

Figure 6. (a, b) ADF-STEM images of ODE-capped Ge nanocrystals obtained from Reaction #7 in Table 1. Twin defects are visible in (c) and (d).

some twin defects. The hexagonal cross-sectional shape is observed when viewed down the [110] zone axis. The Raman spectra in Figure 7 exhibit peaks appear near the expected crystalline Ge−Ge transverse optical (TO) phonon mode at 298 cm^{-1}.[S1] As the nanocrystal size decreases, The Raman peak shifts to lower energy from 298.8 to 292.1 cm^{-1} with asymmetric peak broadening as the nanocrystal size decreases. This well-known size effect results as phonon modes away from the Brillouin zone center become increasingly allowed in the CQDs.[S2−S4]

https://doi.org/10.1021/jacs.4c13692
J. Am. Chem. Soc. 2025, 147, 1792−1802

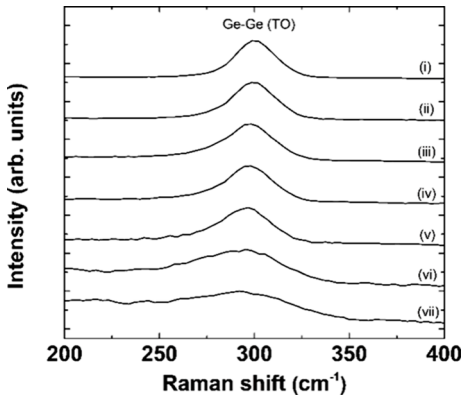

Figure 7. Raman spectra for Ge nanocrystals with different diameters: (i) 17.8 ± 1.8, (ii) 15.4 ± 1.9, (iii) 11.8 ± 1.2, (iv) 10.2 ± 1.1, (v) 8.8 ± 0.8, (vi) 6.2 ± 0.8, and (vii) 3.0 ± 0.2 nm. Changes in Raman signal due to laser exposure (λ_{exc} = 532 nm, 7 mW) were avoided by acquiring the Raman signal immediately after exposing the sample to the laser. Raman spectra were acquired for 5 s.

3.2. Nanocrystal Growth Mechanism. Figure 1 illustrates the reaction pathway for the Ge nanocrystals. As the temperature increases, the reaction solution changes color from orange to black around 150 °C as Ge nanocrystals nucleate and begin to grow. The exact temperature of the color change depended on the precursor concentration and the ligand chemistry. The presence of TOP and ODE significantly alter the nanocrystal nucleation and growth kinetics. TOP for example disrupts the Ge-OAm bonding and raises the temperature needed for reactant decomposition. Consequently, nucleation at the higher temperature results in the formation of larger nanocrystals due to the increased growth rate. Eqs 4−6 highlight the key chemical reactions involved in process.

$$GeI_2 + cRNH_2 \rightarrow Ge(NHR)_a(NH_2R)_bI_{2-a-b} + aNH_3R^+I^- \quad (4)$$

$$2[Ge(II)] \xrightarrow{Heat} [Ge^0] + [Ge(IV)] \quad (5)$$

$$Ge^0(OAm)_x + y\text{ODE} + H^+ \rightarrow Ge^0(\text{ODE}) + y\text{OAm} \quad (6)$$

OAm can serve as an *L*-type or *X*-type ligand by forming either Ge-amine or Ge-amide linkages that are reversible.[55−57] Ge-OAm complexation (eq 4) also helps initiate nanocrystal growth by reducing the energy barrier of the GeI_2 disproportionation reaction (eq 5).[23] Once the temperature reaches 260 °C, the OAm capping ligands are replaced by ODE (eq 6) (see Supporting Information, Figures S3 and S9). Alkenes typically add to Ge surfaces by a hydrogermylation reaction, and for this to occur, there must be a source of H in the reaction.[58] OAm most likely also serves as a source of H for the addition of the alkene to the Ge surface.[59] The irreversible covalent Ge−C bonding of the ligands then prevents further nanocrystal growth.

3.3. Nanocrystal Surface Characteristics. To confirm that ODE displaces OAm capping ligands during synthesis, the nanocrystals were examined by ^{1}H NMR spectroscopy. Figure 8 shows ^{1}H NMR spectra of Ge nanocrystals prepared in OAm with and without ODE. Both sets of nanocrystal spectra exhibit the significantly broadened peaks characteristic of surface-bound capping ligands.[60,61] Nanocrystals synthesized without ODE had spectra with the characteristic resonances of vinylic protons of OAm at δ 5.36 ppm and protons neighboring the double bond at δ 2.00 ppm.[62] Resonances at δ 1.00, and δ 2.67 ppm, corresponding to the α-protons and β-protons associated with the amine group of OAm, are not observed—indicating that they are close to the Ge surface and immobilized within the capping ligand layer.[60,61]

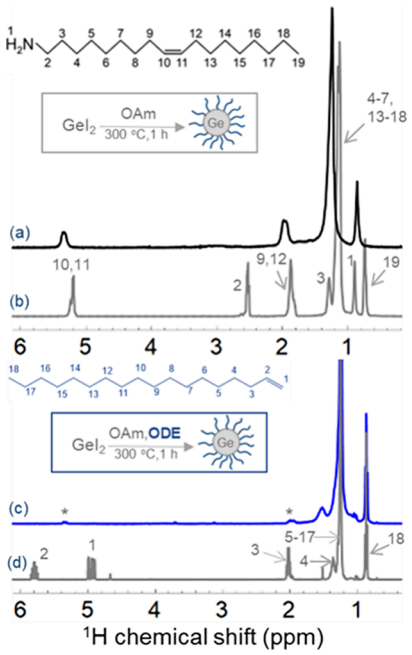

Figure 8. ^{1}H NMR spectra of Ge nanocrystals synthesized in (a) OAm and (c) OAm with added ODE dispersed in chloroform-*d*. Spectra for (b) pure OAm and (d) ODE in chloroform-*d* are also shown. The asterisk symbol (*) in (c) denotes protons associated with double bond in trace amount of residual OAm.

As Figure 8 shows, when ODE was present in the reaction, the Ge nanocrystals no longer show the ^{1}H NMR peaks corresponding to the OAm double bond at δ 5.36 (vinylic protons) and 2.00 ppm (protons neighboring the double bond). The broadened methyl δ 0.88 ppm and methylene δ 1.25 ppm resonances are present, while the vinylic protons of ODE at δ 5.0 ppm and δ 5.8 ppm are not observed. This indicates that ODE has bonded to the nanocrystals via the double bond by hydrogermylation with the Ge surface.

Figure 9 shows FTIR spectra for Ge nanocrystals synthesized in OAm with and without added ODE. The spectrum of the nanocrystals synthesized without ODE shows stretching vibrations characteristic of OAm of −NH, =CH, −CH, and C=C groups at 3320, 3008, 2925, and 1562 cm^{-1} as well as bending vibrations of −NH and −CH groups at 1641 and 1465 cm^{-1}.[28,63] The nanocrystals obtained with added ODE do not show any of the peaks associated with −NH stretching, =CH stretching, C=C stretching, and −NH bending vibrations. A peak corresponding to the Ge−C stretching vibration at 700 cm^{-1} is visible.[3,63] These spectra further confirm that OAm is displaced with ODE during the synthesis. The nanocrystals synthesized with ODE present are also significantly more hydrophobic than the OAm-capped nanocrystals, as shown in Figure 9. The contact angles of a sessile water droplet on films of Ge nanocrystals synthesized in OAm with and without ODE were 102.9° and 80.2°,

https://doi.org/10.1021/jacs.4c13692
J. Am. Chem. Soc. 2025, 147, 1792−1802

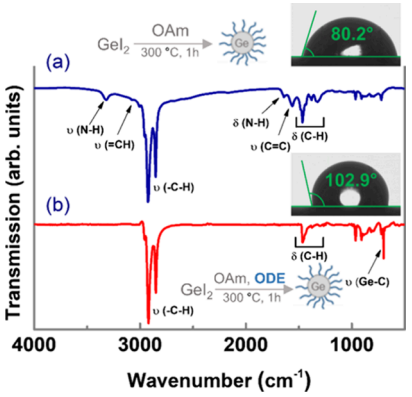

Figure 9. FTIR spectra of Ge nanocrystals synthesized in OAm (a) without and (b) with ODE. (Insets) Images of sessile water droplets on films of OAm- and ODE-capped Ge nanocrystals drop-cast on Si wafers to obtain contact angles.

respectively. This results in part from the more polar bonding between the amine and the Ge surface compared to the Ge−C bonded capping ligands.

Ge nanocrystals synthesized with ODE were also much less susceptible to oxidation than the OAm-capped nanocrystals. Figure 10 shows images of Ge nanocrystals dispersed in

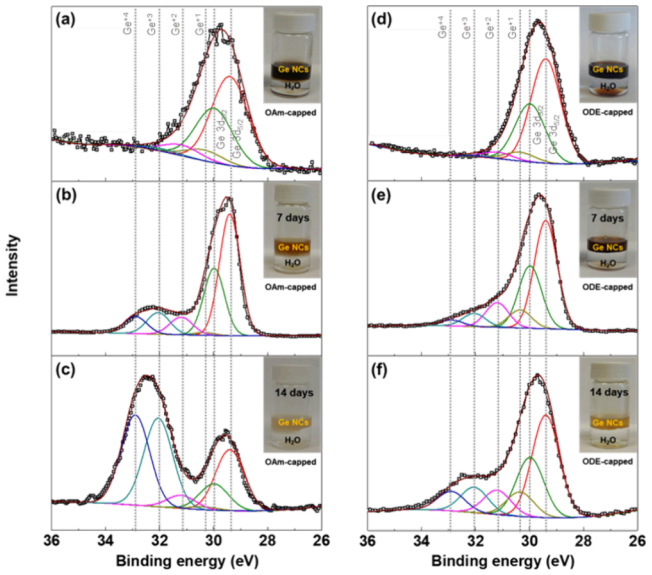

Figure 10. Ge 3d XPS of Ge nanocrystals synthesized in OAm (a−c) without and (d−f) with added ODE that were dispersed in toluene and contacted with water for 14 days. (Insets) Photographs of vials of Ge nanocrystals dispersed in toluene and contacted with water. The nanocrystals change color as they oxidize.

toluene that were contacted with water in air for 14 days and Ge 3d XPS data. The nanocrystals lose their dark brown color and become yellow over time as they oxidize. XRD data are provided in Supporting Information (Figure S7). The nanocrystal spectra show the characteristic doublet for Ge^0 with $3d_{3/2}$ (29.4 eV) and $3d_{5/2}$ (30.0 eV) spin−orbit splitting of 0.6 eV.[36,38] As the nanocrystals oxidize, additional XPS peaks show up at higher energy. The XPS data in Figure 10 are deconvoluted using four peaks shifted by 0.85 eV per Ge−O bond or oxidation state.[64] Both sets of nanocrystals oxidize over time, but the nanocrystals synthesized without ODE are more susceptible to oxidation.

3.4. Optical Properties. Figure 11 shows UV-vis-NIR absorbance and PL spectra of Ge nanocrystals spanning a wide

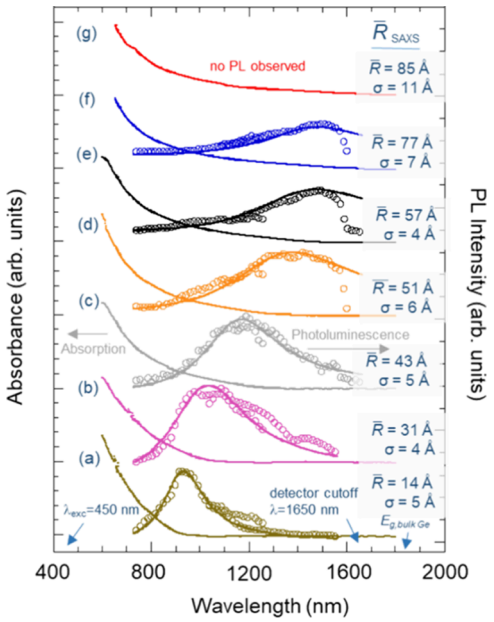

Figure 11. (a) Room-temperature UV-vis-NIR absorbance and PL emission (λ_{exc} = 450 nm) spectra of Ge nanocrystals dispersed in TCE. Nanocrystals were synthesized in mixtures of OAm, ODE, and TOP. The average radii, $\bar{R}$, and the standard deviations, σ, were determined by SAXS. The full PL spectra for the larger nanocrystals are limited by the detector cutoff at around 1650 nm. Solid lines are provided as Gaussian fits of the PL spectra based on photon energy to determine the peak maxima. See Supporting Information Table S1 for a summary of the absorption onsets, PL peak positions, and PL quantum yields and Figure S12 for a comparison of the size-dependent PL peak positions with the values expected based on the effective mass approximation.

range of sizes. The featureless absorbance spectra are characteristic of the indirect band gap of Ge, similar to Si.[65] The optical absorption edge and PL peak shift to higher energy with decreasing particle size due to quantum confinement (see Supporting Information, Figure S10). No green PL associated with GeO_x surface states[39,40] was observed for these samples. (Surface GeO_x can produce a weak green fluorescence, which does not change in energy with size.)[2,6,28,39,40] The highest PL QY for these samples was 0.02%, which was observed for the smallest nanocrystals. Although the PL QY is not high, PL could be observed with an IR camera (see Supporting Information in Figure S11). A PL QY for Ge nanocrystals has reported to be as high as 8% in the shorter wavelength NIR spectral region, but QYs reported in other studies have been much lower—less than 1%.[3,8,44]

The PL QY decreased as the particle size increased and no PL could be detected from the largest nanocrystals with 17 nm diameter. Decreased quantum yields for larger nanocrystals has been reported in many infrared-emitting nanocrystals such as HgTe and PbSe materials.[66−69] Trap sites can lower the PL efficiency by providing alternative pathways for nonradiative recombination. Another possible explanation for this trend is PL quenching due to the energy transfer to vibrational modes of the passivating ligands.[8]

https://doi.org/10.1021/jacs.4c13692
J. Am. Chem. Soc. 2025, 147, 1792−1802

Figure 12 shows temperature-dependent PL spectra for 8.8 nm diameter ODE-capped Ge nanocrystals. PL efficiency

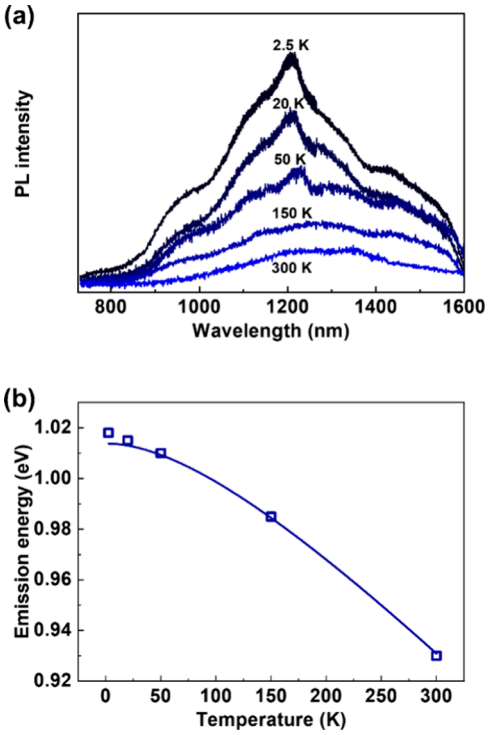

Figure 12. (a) Temperature-dependent PL emission spectra (λ_{exc} = 450 nm) of 8.8 nm diameter ODE-capped Ge nanocrystals on a sapphire substrate. (b) PL peak positions as a function of temperature. The emission energy is fitted to the Varshni equation.

usually increases with decreasing temperature due to slower trap-assisted recombination.[70,71] Temperature-dependent PL of the Ge nanocrystals was further studied from 2.5 to 300 K. Due to the thermal expansion and exciton−phonon interaction, the blue shift of the PL peaks was observed with decreasing temperature. The peak position was fitted using the Varshni equation:

$$E(T) = E(0) - \alpha T^2/(T + \beta) \quad (7)$$

where E (0) is the band gap at 0 K, α is Varshni's coefficient, and β is the Debye temperature.[72] Assuming Ge nanocrystals have the same parameters as bulk Ge ($\alpha = 4.7 \times 10^{-4}$ eV/K, β = 210 K), the PL peak positions were plotted as a function of temperature.[73] The best fit was achieved when E (0) was 1.014 eV, and the temperature-dependent shift followed the Varshni's empirical expression. Moreover, the PL intensity increased significantly as the temperature decreased. Both nonradiative trap-assisted recombination and PL quenching due to energy transfer to the vibrational modes of the ligands are suppressed at low temperature.

4. CONCLUSIONS

Alkyl-passivated Ge nanocrystals were synthesized with a wide range of sizes, from 3−18 nm, using a relatively straightforward heat-up method. In this one-pot synthesis, OAm serves as a source of Ge-amine complexes to initiate the particle growth. As the temperature increases, labile OAm capping ligands are replaced by ODE, as confirmed by ^{1}H NMR and FTIR spectra. The ODE-capped Ge nanocrystals are more hydrophobic and resistant to oxidation than OAm nanocrystals, as ODE forms irreversible covalent Ge−C bonds with the Ge surface via a hydrogermylation reaction. Size control is achieved by modifying the reactant ratios, reaction temperature, and heat-up rate. Band edge PL could be widely tuned by size across the IR spectral region from the bulk band gap of Ge without any GeO_x trap-related green fluorescence. The ability to tune the PL of Ge nanocrystals by size with stability to oxidation is a prerequisite for applications such as biological imaging in the NIR-II spectral region. Further work is required to further improve the PL QYs, perhaps by the addition of an inorganic shell.

■ ASSOCIATED CONTENT

Supporting Information

The Supporting Information is available free of charge at https://pubs.acs.org/doi/10.1021/jacs.4c13692.

Photographs of color change in Ge solution; TEM images of Ge nanocrystals with various experimental conditions; an SEM image of Ge nanocrystals; XRD patterns of oxidized Ge nanocrystals; TGA of OAm- and ODE-capped Ge nanocrystals; ^{1}H NMR spectra of Ge nanocrystals synthesized at different temperatures; Tauc plots of the Ge nanocrystals; IR camera image of Ge nanocrystals; and comparison of the size-dependent optical properties with other experimental results and the effective mass approximation and tight-binding model calculations (PDF)

■ AUTHOR INFORMATION

Corresponding Author

Brian A. Korgel − *McKetta Department of Chemical Engineering and Texas Material Institute, The University of Texas at Austin, Austin, Texas 78712, United States;* orcid.org/0000-0001-6242-7526; Phone: +1-512-471-5633; Email: korgel@che.utexas.edu; Fax: +1-512-471-7060

Authors

Jungchul Noh − *McKetta Department of Chemical Engineering and Texas Material Institute, The University of Texas at Austin, Austin, Texas 78712, United States*

Hyun Gyung Kim − *McKetta Department of Chemical Engineering and Texas Material Institute, The University of Texas at Austin, Austin, Texas 78712, United States*

Daniel W. Houck − *McKetta Department of Chemical Engineering and Texas Material Institute, The University of Texas at Austin, Austin, Texas 78712, United States;* orcid.org/0000-0002-3583-0595

Tushti Shah − *McKetta Department of Chemical Engineering and Texas Material Institute, The University of Texas at Austin, Austin, Texas 78712, United States;* orcid.org/0000-0002-7334-1979

Yangning Zhang − *McKetta Department of Chemical Engineering and Texas Material Institute, The University of Texas at Austin, Austin, Texas 78712, United States;* orcid.org/0000-0001-5511-955X

Alexandra Brumberg − *Department of Chemistry, Northwestern University, Evanston, Illinois 60208, United States;* orcid.org/0000-0003-2512-4686

Richard D. Schaller − *Department of Chemistry, Northwestern University, Evanston, Illinois 60208, United*

https://doi.org/10.1021/jacs.4c13692
J. Am. Chem. Soc. 2025, 147, 1792−1802

States; Center for Nanoscale Materials, Argonne National Laboratory, Lemont, Illinois 60439, United States

Complete contact information is available at: https://pubs.acs.org/10.1021/jacs.4c13692

Notes

The authors declare no competing financial interest.

■ ACKNOWLEDGMENTS

Financial support for this work was provided by the Robert A. Welch Foundation (F-1464), the National Science Foundation Industry/University Cooperative Research Center on Next Generation Photovoltaics (IIP-1540028, IIP-1822206), and the National Science Foundation (CBET-1624659). Work performed at the Center for Nanoscale Materials, a U.S. Department of Energy Office of Science User Facility, was supported by the U.S. DOE, Office of Basic Energy Sciences, under Contact No. DE-AC02-06CH11357. We acknowledge support of the National Science Foundation MSN Program Award CHE-2305121 (A.B. and R.D.S) and the National Science Foundation Graduate Research Fellowship Program under Grant DGE-1842165 (A.B.).

■ REFERENCES

(1) Heath, J. R.; Shiang, J. J.; Alivisatos, A. P. Germanium Quantum Dots: Optical Properties and Synthesis. *J. Chem. Phys.* **1994**, *101*, 1607−1615.

(2) Takeoka, S.; Fujii, M.; Hayashi, S.; Yamamato, K. Size-Dependent Near-Infrared Photoluminescence from Ge Nanocrystals Embedded in SiO_2 Matrices. *Phys. Rev. B* **1998**, *58*, 7921−7925.

(3) Lee, D. C.; Pietryga, J. M.; Robel, I.; Werder, D. J.; Schaller, R. D.; Klimov, V. I. Colloidal Synthesis of Infrared-Emitting Germanium Nanocrystals. *J. Am. Chem. Soc.* **2009**, *131*, 3436−3437.

(4) Vitiello, E.; Schreiber, C. H.; Riccardi, E. X.; Nedell, J. G.; Bellincioni, E.; Parravicini, J.; Binetti, S. O.; Podestà, A.; Lenardi, C.; Pezzoli, F.; Vece, M. D. Inserting Hydrogen into Germanium Quantum Dots. *J. Phys. Chem. C* **2021**, *125*, 24640−24647.

(5) Vaughn, D. D., II; Schaak, R. E. Synthesis, Properties and Applications of Colloidal Germanium and Germanium-Based Nanomaterials. *Chem. Soc. Rev.* **2013**, *42*, 2861−2879.

(6) Pescara, B.; Mazzio, K. A. Morphological and Surface-State Challenges in Ge Nanoparticle Applications. *Langmuir* **2020**, *36*, 11685−11701.

(7) Carolan, D. Recent Advances in Germanium Nanocrystals: Synthesis, Optical Properties and Applications. *Prog. Mater. Sci.* **2017**, *90*, 128−158.

(8) Robel, I.; Shabaev, A.; Lee, D. C.; Schaller, R. D.; Pietryga, J. M.; Crooker, S. A.; Efros, A. L.; Klimov, V. I. Temperature and Magnetic-Field Dependence of Radiative Decay in Colloidal Germanium Quantum Dots. *Nano Lett.* **2015**, *15*, 2685−2692.

(9) Ju, Z.; Qi, X.; Sfadia, R.; Wang, M.; Tseng, E.; Panchul, E. C.; Carter, S. A.; Kauzlarich, S. M. Single-Crystalline Germanium Nanocrystals via a Two-Step Microwave-Assisted Colloidal Synthesis from GeI_4. *ACS Mater. Au* **2022**, *2*, 330−342.

(10) Parravicini, J.; Trapani, F. D.; Nelson, M. D.; Rex, Z. T.; Beiter, R. D.; Catelani, T.; Acciarri, M. F.; Podesta, A.; Lenardi, C.; Binetti, S. O.; Vece, M. D. Quantum Confinement in the Spectral Response of n-Doped Germanium Quantum Dots Embedded in an Amorphous Si Layer for Quantum Dot-Based Solar Cells. *ACS Appl. Nano Mater.* **2020**, *3*, 2813−2821.

(11) Wang, K.; Xu, G.; Gao, F.; Liu, H.; Ma, R.-L.; Zhang, X.; Wang, Z.; Cao, G.; Wang, T.; Zhang, J.-J.; Culcer, D.; Hu, X.; Jiang, H.-W.; Li, H.-O.; Guo, G.-C.; Guo, G.-P. Ultrafast Coherent Control of a Hole Spin Qubit in a Germanium Quantum Dots. *Nat. Commun.* **2022**, *13*, 206.

(12) Peng, Y.; Miao, L.; Liu, C.; Song, H.; Kurosawa, M.; Nakatsuka, O.; Back, S. Y.; Rhyee, J. S.; Murata, M.; Tanemura, S.; Baba, T.; Baba, T.; Ishizaki, T.; Mori, T. Constructed Ge Quantum Dots and Sn Precipitate SiGeSn Hybrid Film with High Thermoelectric Performance at Low Temperature Region. *Adv. Energy Mater.* **2022**, *12*, No. 2103191.

(13) Foerester, A.; Besley, N. A. Quantum Chemical Characterization and Design of Quantum Dots for Sensing Applications. *J. Phys. Chem. A* **2022**, *126*, 2899−2908.

(14) Rauter, P.; Spindlberger, L.; Schaffler, F.; Fromherz, T.; Freund, J.; Brehm, M. Room-Temperature Group-IV LED Based on Defect-Enhanced Ge Quantum Dots. *ACS Photonics* **2018**, *5*, 431−438.

(15) Niquet, Y. M.; Allan, G.; Delerue, C.; Lannoo, M. Quantum Confinement in Germanium Nanocrystals. *Appl. Phys. Lett.* **2000**, *77*, 1182−1184. Carolan, D.; Doyle, H. Efficient One-Pot Synthesis of Monodisperse Alkyl-Terminated Colloidal Germanium Nanocrystals. *J. Nanopart. Res.* **2014**, *16*, 2721.

(16) Chou, N. H.; Oyler, K. D.; Motl, N. E.; Schaak, R. E. Colloidal Synthesis of Germanium Nanocrystals Using Room-Temperature Benchtop Chemistry. *Chem. Mater.* **2009**, *21*, 4105−4107.

(17) Prabakar, S.; Shiohara, A.; Hanada, S.; Fujioka, K.; Yamamoto, K.; Tilley, R. D. Size Controlled Synthesis of Germanium Nanocrystals by Hydride Reducing Agents and Their Biological Applications. *Chem. Mater.* **2010**, *22*, 482−486.

(18) Warner, J. H.; Tilley, R. D. Synthesis of Water-Soluble Photoluminescent Germanium Nanocrystals. *Nanotechnology* **2006**, *17*, 3745−3749.

(19) Karatutlu, A.; Song, M.; Wheeler, A. P.; Ersoy, O.; Little, W. R.; Zhang, Y.; Puech, P.; Boi, F. S.; Luklinska, Z.; Sapelkin, A. V. Synthesis and Structure of Free-Standing Germanium Quantum Dots and Their Application in Live Cell Imaging. *RSC Adv.* **2015**, *5*, 20566−20573.

(20) Lu, X. M.; Korgel, B. A.; Johnston, K. P. High Yield of Germanium Nanocrystals Synthesized from Germanium Diiodide in Solution. *Chem. Mater.* **2005**, *17*, 6479−6485.

(21) Gerung, H.; Bunge, S. D.; Boyle, T. J.; Brinker, C. J.; Han, S. M. Anhydrous Solution Synthesis of Germanium Nanocrystals from the Germanium (II) Precursor $Ge[N(SiMe_3)_2]_2$. *Chem. Commun.* **2005**, 1914−1916.

(22) Muthuswamy, E.; Zhao, J.; Tabatabaei, K.; Amador, M. M.; Holmes, M. A.; Osterloh, F. E.; Kauzlarich, S. M. Thiol-Capped Germanium Nanocrystals: Preparation and Evidence for Quantum Size Effects. *Chem. Mater.* **2014**, *26*, 2138−2146.

(23) Ruddy, D. A.; Johnson, J. C.; Smith, R.; Neale, N. R. Size and Bandgap Control in the Solution-Phase Synthesis of Near-Infrared-Emitting Germanium Nanocrystals. *ACS Nano* **2010**, *4*, 7459−7466.

(24) Armatas, G. S.; Kanatzidis, M. G. High-Surface-Area Mesoporous Germanium from Oxidative Polymerization of the Deltahedral $[Ge_9]^{4-}$ Cluster: Electronic Structure Modulation with Donor and Acceptor Molecules. *Adv. Mater.* **2008**, *20*, 546−550.

(25) Zaitseva, N.; Dai, Z. R.; Grant, C. D.; Harper, J.; Saw, C. Germanium Nanocrystals Synthesized in High-Boiling-Point Organic Solvents. *Chem. Mater.* **2007**, *19*, 5174−5178.

(26) Warner, J. H. Solution-Phase Synthesis of Germanium Nanoclusters Using Sulfur. *Nanotechnology* **2006**, *17*, 5613−5619.

(27) Nolan, B. M.; Chan, E. K.; Zhang, X.; Muthuswamy, E.; van Benthem, K.; Kauzlarich, S. M. Sacrificial Silver Nanoparticles: Reducing GeI_2 to Form Hollow Germanium Nanoparticles by Electroless Deposition. *ACS Nano* **2016**, *10*, 5391−5397.

(28) Henderson, E. J.; Hessel, C. M.; Veinot, J. G. C. Synthesis and Photoluminescent Properties of Size-Controlled Germanium Nanocrystals from Phenyl Trichlorogermane-Derived Polymers. *J. Am. Chem. Soc.* **2008**, *130*, 3624−3632.

(29) Hoffman, M.; Veinot, J. G. C. Understanding the Formation of Elemental Germanium by Thermolysis of Sol-Gel Derived Organogermanium Oxide Polymers. *Chem. Mater.* **2012**, *24*, 1283−1291.

(30) Gresback, R.; Holman, Z.; Kortshagen, U. Nonthermal Plasma Synthesis of Size-Controlled, Monodisperse, Freestanding Germanium Nanocrystals. *Appl. Phys. Lett.* **2007**, *91*, No. 093119.

(31) Zhu, X.; ten Brink, G. H.; de Graaf, S.; Kooi, B. J.; Palasantzas, G. Gas-Phase Synthesis of Tunable-Size Germanium Nanocrystals by Inert Gas Condensation. *Chem. Mater.* **2020**, *32*, 1627−1635.
(32) Malekzadeh, M.; Swihart, M. T. Vapor-Phase Production of Nanomaterials. *Chem. Soc. Rev.* **2021**, *50*, 7132−7249.
(33) Nadalini, G.; Borghi, F.; Piseri, P.; Di Vece, M. Persistent Quantum Confinement in a Germanium Quantum Dot Solid. *Phys. E* **2023**, *151*, No. 115708.
(34) Meng, A. C.; Fenrich, C. S.; Braun, M. R.; McVittie, J. P.; Marshall, A. F.; Harris, J. S.; McIntyre, P. C. Core/Shell Germanium/Germanium-Tin Nanowires Exhibiting Room Temperature Direct- and Indirect-Gap Photoluminescence. *Nano Lett.* **2016**, *16*, 7521−7529.
(35) Biswas, S.; Doherty, J.; Saladukha, D.; Ramasse, Q.; Majumdar, D.; Upmanyu, M.; Singha, A.; Ochalski, T.; Morris, M. A.; Holmes, J. D. Non-Equilibrium Induction of Tin in Germanium: Towards Direct Bandgap $Ge_{1-x}Sn_x$ Nanowires. *Nat. Commun.* **2016**, *7*, 11405.
(36) Hanrath, T.; Korgel, B. A. Chemical Surface Passivation of Ge Nanowires. *J. Am. Chem. Soc.* **2004**, *126*, 15466−15472.
(37) Lu, X.; de la Mata, M.; Arbiol, J.; Korgel, B. A. Colloidal Silicon-Germanium Nanorod Heterostructures. *Chem. Mater.* **2017**, *29*, 9786−9792.
(38) Holmberg, V. C.; Korgel, B. A. Corrosion Resistance of Thiol- and Alkene-Passivated Germanium Nanowires. *Chem. Mater.* **2010**, *22*, 3698−3703.
(39) Shirahata, N.; Hirakawa, D.; Masuda, Y.; Sakka, Y. Size-Dependent Color Tuning of Efficiently Luminescent Germanium Nanoparticles. *Langmuir* **2013**, *29*, 7401−7410.
(40) Rodio, M.; Scarpellini, A.; Diaspro, A.; Intartaglia, R. Tailoring of Size, Emission, and Surface Chemistry of Germanium Nanoparticles *via* Liquid-Phase Picosecond Laser Ablation. *J. Mater. Chem. C* **2017**, *46*, 12264.
(41) Das, S.; Aluguri, R.; Manna, S.; Singha, R.; Dhar, A.; Pavesi, L.; Ray, S. K. Optical and Electrical Properties of Undoped and Doped Ge Nanocrystals. *Nanoscale Res. Lett.* **2012**, *7*, 143.
(42) Wheeler, L. M.; Levij, L. M.; Kortshagen, U. R. Tunable Band Gap Emission and Surface Passivation of Germanium Nanocrystals Synthesized in the Gas Phase. *J. Phys. Chem. Lett.* **2013**, *4*, 3392−3396.
(43) Boote, B. W.; Men, L.; Andaraarachchi, H. P.; Bhattacharjee, U.; Petrich, J. W.; Vela, J.; Smith, E. A. Germanium-Tin/Cadmium Sulfide Core/Shell Nanocrystals with Enhanced Near-Infrared Photoluminescence. *Chem. Mater.* **2017**, *29*, 6012−6021.
(44) Guo, Y.; Rowland, C. E.; Schaller, R. D.; Vela, J. Near-Infrared Photoluminescence Enhancement in Ge/CdS and Ge/ZnS Core/Shell Nanocrystals: Utilizing IV/II-VI Semiconductor Epitaxy. *ACS Nano* **2014**, *8*, 8334−8343.
(45) Kerr, A. T.; Placencia, D.; Gay, M. E.; Boercker, J. E.; Soto, D.; Davis, M. H.; Banek, N. A.; Foos, E. E. Sulfur-Capped Germanium Nanocrystals: Facile Inorganic Ligand Exchange. *J. Phys. Chem. C* **2017**, *121*, 22597−22606.
(46) Yu, H.; Helbich, T.; Scherf, L. M.; Chen, J.; Cui, K.; Fässler, T. F.; Rieger, B.; Veinot, J. G. C. Radical-Initiated and Thermally Induced Hydrogermylation of Alkenes on the Surfaces of Germanium Nanosheets. *Chem. Mater.* **2018**, *30*, 2274−2280.
(47) Korgel, A. B.; Fullam, S.; Connolly, S.; Fitzmaurice, D. Assembly and Self-Organization of Silver Nanocrystal Superlattice: Ordered "Soft Spheres". *J. Phys. Chem. B* **1998**, *102*, 8379−8388.
(48) Guillaussier, A.; Yu, Y.; Voggu, V. R.; Aigner, W.; Cabezas, C. S.; Houck, D. W.; Shah, T.; Smilgies, D.-M.; Pereira, R. N.; Stutzmann, M.; Korgel, B. A. Silicon Nanocrystal Superlattice Nucleation and Growth. *Langmuir* **2017**, *33*, 13068−13076.
(49) Mattoussi, H.; Cumming, A. W.; Murray, C. B.; Bawendi, M. G.; Ober, R. Characterization of CdSe Nanocrystallite Dispersions by Small Angle X-ray Scattering. *J. Chem. Phys.* **1996**, *105*, 9890−9896.
(50) Saunders, A. E.; Korgel, B. A. Second Virial Coefficient Measurements of Dilute Gold Nanocrystal Dispersions Using Small-Angle X-ray Scattering. *J. Phys. Chem. B* **2004**, *108*, 16731−16738.
(51) Saeed, S.; de Weerd, C.; Stallinga, P.; Spoor, F. CM.; Houtepen, A. J.; Siebbeles, L. DA.; Gregorkiewicz, T. Carrier Multiplication in Germanium Nanocrystals. *Light: Sci. Appl.* **2015**, *4*, No. e251.
(52) Hessel, C. M.; Wei, J.; Reid, D.; Fujii, H.; Downer, M. C.; Korgel, B. A. Raman Spectroscopy of Oxide-Embedded and Ligand-Stabilized Silicon Nanocrystals. *J. Phys. Chem. Lett.* **2012**, *3*, 1089−1093.
(53) Richter, H.; Wang, Z. P.; Ley, L. The One Phonon Raman Spectrum in Microcrystalline Silicon. *Solid State Commun.* **1981**, *39*, 625−629.
(54) Muthuswamy, E.; Iskandar, A. S.; Amador, M. M.; Kauzlarich, S. M. Facile Synthesis of Germanium Nanoparticles with Size Control: Microwave *versus* Conventional Heating. *Chem. Mater.* **2013**, *25*, 1416−1422.
(55) He, M.; Protesescu, L.; Caputo, R.; Krumeich, F.; Kovalenko, M. V. A General Synthesis Strategy for Monodisperse Metallic and Metalloid Nanoparticles (In, Ga, Bi, Sb, Zn, Cu, Sn, and Their Alloys) via in Situ Formed Metal Long-Chain Amides. *Chem. Mater.* **2015**, *27*, 635−647.
(56) Wheeler, L. M.; Nichols, A. W.; Chernomordik, B. D.; Anderson, N. C.; Beard, M. C.; Neale, N. R. All-Inorganic Germanium Nanocrystal Films by Cationic Ligand Exchange. *Nano Lett.* **2016**, *16*, 1949−1954.
(57) Ruddy, D. A.; Erslev, P. T.; Habas, S. E.; Seabold, J. A.; Neale, N. R. Surface Chemistry Exchange of Alloyed Germanium Nanocrystals: A Pathway Toward Conductive Group IV Nanocrystal Films. *J. Phys. Chem. Lett.* **2013**, *4*, 416−421.
(58) Choi, K.; Buriak, J. M. Hydrogermylation of Alkenes and Alkynes on Hydride-Terminated Ge (100) Surfaces. *Langmuir* **2000**, *16*, 7737−7741.
(59) Tabatabaei, K.; Holmes, A. L.; Newton, K. A.; Muthuswamy, E.; Sfadia, R.; Carter, S. A.; Kauzlarich, S. M. Halogen-Induced Crystallinity and Size Tuning of Microwave Synthesized Germanium Nanocrystals. *Chem. Mater.* **2019**, *31*, 7510−7521.
(60) Badia, A.; Gao, W.; Singh, S.; Demers, L.; Cuccia, L.; Reven, L. Structure and Chain Dynamics of Alkanethiol-Capped Gold Colloids. *Langmuir* **1996**, *12*, 1262−1269.
(61) Hens, Z.; Martins, J. C. A Solution NMR Toolbox for Characterizing the Surface Chemistry of Colloidal Nanocrystals. *Chem. Mater.* **2013**, *25*, 1211−1221.
(62) Houck, D. W.; Korgel, B. A. Facile Exchange of Tightly Bonded L-Type Oleylamine and Diphenylphosphine Ligands on Copper Indium Diselenide Nanocrystals Mediated by Molecular Iodine. *Chem. Mater.* **2018**, *30*, 8359−8367.
(63) McVey, B. F. P.; O'Mara, P. B. O.; McGrath, A. J.; Faramus, A.; Yasarapudi, V. B.; Goncales, V. R.; Tan, V. T. G.; Schmidt, T. W.; Gooding, J. J.; Tilley, R. D. Role of Surface Capping Molecule Polarity on the Optical Properties of Solution Synthesized Germanium Nanocrystals. *Langmuir* **2017**, *33*, 8790−8798.
(64) Schmeisser, D.; Schnell, R. D.; Bogen, A.; Himpsel, F. J.; Rieger, D.; Landgren, G.; Morar, J. F. Surface Oxidation States of Germanium. *Surf. Sci.* **1986**, *172*, 455−465.
(65) Hessel, C. M.; Reid, D.; Panthani, M. G.; Rasch, M. R.; Goodfellow, B. W.; Wei, J.; Fujii, H.; Akhavan, V.; Korgel, B. A. Synthesis of Ligand-Stabilized Silicon Nanocrystals with Size-Dependent Photoluminescence Spanning Visible to Near-Infrared Wavelengths. *Chem. Mater.* **2012**, *24*, 393−401.
(66) Keuleyan, S.; Kohler, J.; Guyot-Sionnest, P. Photoluminescence of Mid-Infrared HgTe Colloidal Quantum Dots. *J. Phys. Chem. C* **2014**, *118*, 2749−2753.
(67) Semonin, O. E.; Johnson, J. C.; Luther, J. M.; Midgett, A. G.; Nozik, A. J.; Beard, M. Absolute Photoluminescence Quantum Yields of IR-26 Dye, PbS, and PbSe Quantum Dots. *J. Phys. Chem. Lett.* **2010**, *1*, 2445−2450.
(68) Liu, H.; Guyot-Sionnest, P. Photoluminescence Lifetime of Lead Selenide Colloidal Quantum Dots. *J. Phys. Chem. C* **2010**, *114*, 14860−14863.

https://doi.org/10.1021/jacs.4c13692
J. Am. Chem. Soc. 2025, 147, 1792−1802

(69) Pietryga, J. M.; Schaller, R. D.; Werder, D.; Stewart, R.; Klimov, V. J.; Hollingsworth, J. A. Pushing the Band Gap Envelope: Mid-Infrared Emitting Colloidal PbSe Quantum Dots. *J. Am. Chem. Soc.* **2004**, *126*, 11752−11753.
(70) Nirmal, M.; Norris, D. J.; Kuno, M.; Bawendi, M. G. Observation of the "Dark Exciton" in CdSe Quantum Dots. *Phys. Rev. Lett.* **1995**, *75*, 3728.
(71) Wen, X.; Dao, L. V.; Hannaford, P. Temperature Dependence of Photoluminescence in Silicon Quantum Dots. *J. Phys. D: Appl. Phys.* **2007**, *40*, 3573−3578.
(72) Das, D.; Shinde, S. L.; Nanda, K. K. Temperature-Dependent Photoluminescence of g-C_3N_4: Implication for Temperature Sensing. *ACS Appl. Mater. Interfaces* **2016**, *8*, 2181−2186.
(73) Varshni, Y. P. Temperature Dependence of the Energy Gap in Semiconductors. *Physica* **1967**, *34*, 149−154.

https://doi.org/10.1021/jacs.4c13692
J. Am. Chem. Soc. 2025, 147, 1792−1802